

Neural Bounding

Stephanie Wenxin Liu
Birkbeck, University of
London
United Kingdom
wenxin.liu.cs@gmail.com

Michael Fischer
University College London
United Kingdom
m.fischer@cs.ucl.ac.uk

Paul D. Yoo
Birkbeck, University of
London
United Kingdom
p.yoo@bbk.ac.uk

Tobias Ritschel
University College London
United Kingdom
t.ritschel@ucl.ac.uk

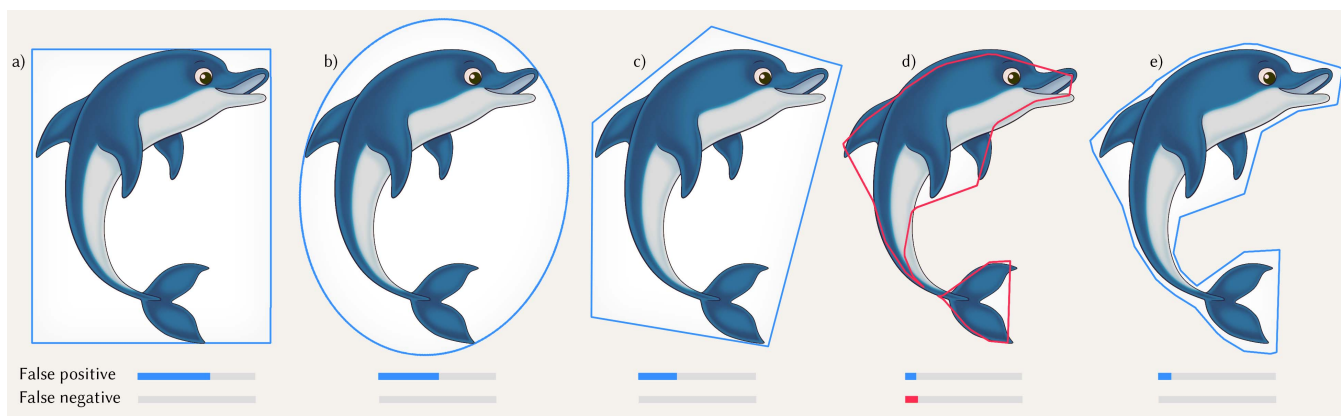


Figure 1: Different bounding volume types classifying 2D space as maybe-object or certainly-not-object, from left to right: box (a), ellipsoid (b), k -oriented planes (c), common neural networks (d) and a neural network trained using our approach (e). While common boundings are not tight, common neural networks are not conservative, missing parts of the dolphin, while ours is both tight and has no false negatives.

ABSTRACT

Bounding volumes are an established concept in computer graphics and vision tasks but have seen little change since their early inception. In this work, we study the use of neural networks as bounding volumes. Our key observation is that bounding, which so far has primarily been considered a problem of computational geometry, can be redefined as a problem of learning to classify space into free or occupied. This learning-based approach is particularly advantageous in high-dimensional spaces, such as animated scenes with complex queries, where neural networks are known to excel. However, unlocking neural bounding requires a twist: allowing – but also limiting – false positives, while ensuring that the number of false negatives is strictly zero. We enable such tight and conservative results using a dynamically-weighted asymmetric loss function. Our results show that our neural bounding produces up to an order of magnitude fewer false positives than traditional methods. In addition, we propose an extension of our bounding method using early exits that accelerates query speeds by 25%. We also demonstrate that our approach is applicable to non-deep

learning models that train within seconds. Our project page is at https://wenxin-liu.github.io/neural_bounding/.

CCS CONCEPTS

• Computing methodologies → Rendering.

KEYWORDS

Neural Primitives, Bounding Primitives, Rendering, Acceleration Structures

ACM Reference Format:

Stephanie Wenxin Liu, Michael Fischer, Paul D. Yoo, and Tobias Ritschel. 2024. Neural Bounding. In *Special Interest Group on Computer Graphics and Interactive Techniques Conference Conference Papers '24 (SIGGRAPH Conference Papers '24)*, July 27-August 1, 2024, Denver, CO, USA. ACM, New York, NY, USA, 10 pages. <https://doi.org/10.1145/3641519.3657442>

1 INTRODUCTION

Efficiently testing two-, three- or higher-dimensional points or ranges for intersections with extended primitives is at the core of many interactive graphics tasks. Examples include testing the 3D position of a particle in a fluid simulation against an animated character mesh, testing rays against a 3D medical scan volume or testing a drone’s flight path against time-varying obstacles.

To accelerate all these queries, it is popular to use a hierarchy of tests: if intersection with a simple *bounding primitive* – such as a box – that conservatively contains a more complex primitive fails, one can skip the costly test with the more complex primitive. For a

Permission to make digital or hard copies of all or part of this work for personal or classroom use is granted without fee provided that copies are not made or distributed for profit or commercial advantage and that copies bear this notice and the full citation on the first page. Copyrights for components of this work owned by others than the author(s) must be honored. Abstracting with credit is permitted. To copy otherwise, or republish, to post on servers or to redistribute to lists, requires prior specific permission and/or a fee. Request permissions from permissions@acm.org.

SIGGRAPH Conference Papers '24, July 27-August 1, 2024, Denver, CO, USA

© 2024 Copyright held by the owner/author(s). Publication rights licensed to ACM.

ACM ISBN 979-8-4007-0525-0/24/07...\$15.00

<https://doi.org/10.1145/3641519.3657442>

correct algorithm, the false-negative (FN) rate of the first test must be zero, i.e., bounding must never miss a true positive intersection.

For efficiency, the main trade-offs are i) the cost of testing the bounding primitive, ii) the cost of intersecting the original primitive, and iii) the false-positive (FP) rate of the bounding primitive. The FP rate measures how often an initial positive intersection with the bounding primitive turns out to be negative upon more detailed testing with the original primitive, leading to wasted computation. A successful bounding method will have both a low testing cost and a low FP rate. Typical bounding solutions include spheres, boxes, oriented boxes or k discretely-oriented polytopes (k -DOPs) [Ericson 2004]. However, fitting those primitives, particularly in higher dimensions, can result in poor FP rates as they remain convex and further may require significant implementation effort [Schneider and Eberly 2002]. In this article, we thus show how to train neural networks to unlock high-dimensional, non-linear, concave bounding with a combination of simplicity, flexibility and testing speed.

While the FP rate is the main concern for *efficiency*, for *correctness* of the bounding algorithm, the challenge is to develop a neural network (NN) that is trained to produce bounds with strictly zero false negatives. This is crucial, as the FN rate quantifies how often the algorithm erroneously classifies an actual intersection as non-intersection – such misclassifications will result in truncated geometry features and cut-off object parts, as exemplified by the fins of the dolphin in Fig. 1, d. A straightforward solution would be to first find a bounding primitive and then compress it using a NN. Another approach would be to learn the NN to approximate the complex primitive and later make the approximation conservative. Instead, we show that with the right initialization and schedule for weighting FPs and FNs, we can incentivize a neural network to become bounding. While our method works well in many cases, we would like to point out that it is a heuristic and thus –not uncommon for neural networks– does not provide strict guarantees.

As it could appear that executing a neural network for testing bounds is too time-intensive to be useful, we carefully study architectures that are both small and simple (inspired by [Reiser et al. 2021] or [Karnewar et al. 2022]), such that they are only slightly more expensive than linear ones or traditional intersection tests. We further demonstrate that our approach is also amenable to optimizing non-neural representations, such as k -DOPs.

We show application to two, three and 4D point queries, 2D and 3D range queries as well as queries of dynamic scenes, including scenes with multiple degrees of freedom, and compare these results to classic bounding methods, such as spheres, boxes and k -DOPs.

2 PREVIOUS WORK

Bounding n -D objects is a core operation in graphics. Classic algorithms can be extremely straightforward, such as axis-aligned boxes, but already fitting a sphere can be more involved than it seems at first. For an established textbook with many bounding and intersection algorithms, see [Schneider and Eberly 2002].

When it comes to bounding complex objects, the situation is more difficult: For a single object that is dominantly convex, k -DOPs have shown useful [Kay and Kajiya 1986; Klosowski et al. 1998]. Another option is to perform convex object-decomposition [Bergen 1997; Ehmann and Lin 2001]. 3D ray-queries, are the most relevant

for such tests, and typically performed on hierarchies, e.g., [Gu et al. 2013; Gunther et al. 2007]; for a survey see Meister et al. [2021].

Recently, NNs have changed many operations in graphics, but notably not bounding. Neural intersection functions (NIFs) [Fujieda et al. 2023] predict intersections and could also be used to intersect boundings, but do not attempt to be conservative, which allows the possibility to miss parts of the object they enclose. Moreover, NIFs are trained on static scenes, requiring a re-training of the networks with each change of scene configuration or camera viewpoint [Fujieda et al. 2023]. Our neural bounding networks, in contrast, are learned on object-level, and hence can easily be rearranged in a scene without retraining, as we show in our experiments. Both our method and NIF are inspired by neural fields, that have successfully modeled occupancy [Mescheder et al. 2019], signed distance and surface distance [Behera and Mishra 2023; Park et al. 2019]. For a comprehensive survey of recent works employing coordinate-based NNs, please see [Xie et al. 2022].

In concurrent work, not specific to rendering, very simple primitives are fitted conservatively to polytopes [Hashimoto et al. 2023], but unable to handle general shapes. Neural concepts have been used to create bounding sphere hierarchies by Weller and colleagues [2014], which uses a neural-inspired optimizer, where the representation of the bounding itself remained classic spheres, while in this article we use non-linear functions. Others [Zesch et al. 2022] attempt to optimize collision testing by replacing the test with a neural network. While that work is similar to ours in the sense that it represents the bounding itself as a non-linear function, it does not strictly bound but simply fits the surface of the indicator with a multi-layer perceptron (MLP) under a common loss. This is also applicable to higher-dimensional spaces (C-spaces) of, e.g., robot configurations [Cai et al. 2022]. Essentially, these methods train signed distance or occupancy functions, but without any special considerations for the difference of FP and FN, which is at the heart of bounding. We compare to such approaches and show that we can combine their advantages with the benefit of never missing an intersection. More advanced, combinations of fields can be learned so as to not collide [Santesteban et al. 2022], but again only by penalizing intersections, not by producing conservative results. Other constraints such as eikonicity [Atzmon and Lipman 2020], Lipschitz continuity [Yariv et al. 2021], or indefinite integrals [Nsampi et al. 2023] can be incentivized similar to how we incentivize conservativeness. Sharp and Jacobsen [Sharp and Jacobson 2022] have proposed a method to query any trained implicit NN over regions using interval arithmetic. That is orthogonal to the question of training the NN to bound a function conservatively, which we study here.

To ensure no FNs, we make use of asymmetric losses, which are typically applied with aims different from ours, such as reducing class imbalance [Ridnik et al. 2021], to become robust to noise [Zhou et al. 2021], to regularize a space [Liu et al. 2023] or, closer to graphics, to control bias and variance in Monte Carlo (MC) path tracing denoisers [Vogels et al. 2018].

3 OUR APPROACH

This section will outline how we construct our networks and the asymmetric loss in order to achieve tight, conservative bounding (strictly zero false negatives) in arbitrary dimensions.

3.1 Method

To achieve our task of conservatively bounding in n -dimensional spaces, we seek to learn a NN that classifies concave regions of space into inside and outside, while ensuring strictly no false negatives. Input to our algorithm is an n -dimensional *indicator* function $f(\mathbf{x}) \in \mathbb{R}^n \rightarrow \{0,1\}$ that returns 1 inside and on the surface of the object, and 0 everywhere else. In 2D, the indicator could be visualized as a regular image grid, a voxel grid in 3D, an animated object in 4D, or a multi-dimensional state space of robot arm poses (or even another network, e.g., a neural density field) in higher dimensions. We assume we can evaluate the indicator function exactly and at arbitrary coordinates. It further is not required to differentiate this function with respect to anything.

On top of the indicator, we define a *query* function $g(\mathbf{r}) \in \mathbb{R}^m \rightarrow \{0,1\}$ that is 1 if the indicator returns 1 for at least one point in the region \mathbf{r} . For point queries, the indicator and query are identical, i.e., $g = f$. For extended queries, such as range queries, \mathbf{r} would be a parameterization of a region, e.g., the two corners defining an axis-aligned bounding box (AABB). While in lower dimensions the indicator and region could be converted into another indicator (akin to the morphological “open” operation on images [Dougherty 1992]), our method also supports queries on high-dimensional indicators that can only be sampled and not be stored in practice.

At the core of our approach is another function $h_\theta(\mathbf{r}) \in \mathbb{R}^m \rightarrow \{0,1\}$, with learnable parameters θ , that is strictly 1 where g is 1, but is allowed to also be 1 in other places (FP). While traditional approaches use computational geometry to infer θ (e.g., via the repeated projection step in k -DOPs or the simple min/max-operation in AABBs), we leverage the power of gradient-based optimization of neural networks to learn the most suitable non-linear h_θ .

The training objective \mathcal{L} to approximate g via h_θ is the combined cost of all FNs and FPs across a region \mathbf{r} :

$$\mathcal{L}(\theta) = \int c(\mathbf{r}) d\mathbf{r}, \quad c(\mathbf{r}) = \begin{cases} 0 & \text{if } g(\mathbf{r}) = 0 \text{ and } h_\theta(\mathbf{r}) = 0, & \text{TN} \\ \alpha & \text{if } g(\mathbf{r}) = 1 \text{ and } h_\theta(\mathbf{r}) = 0, & \text{FN} \\ \beta & \text{if } g(\mathbf{r}) = 0 \text{ and } h_\theta(\mathbf{r}) = 1, & \text{FP} \\ 0 & \text{if } g(\mathbf{r}) = 1 \text{ and } h_\theta(\mathbf{r}) = 1, & \text{TP} \end{cases},$$

where α is the cost for false-negative, which needs to be $\alpha = \infty$ to be conservative, and β is the cost for a false-positive, which we define to be 1. The first and last clause are true positive and negative and incur no cost, while the second clause ensures conservativeness, and the third ensures that the bounding is tight.

However, it is not obvious how to proceed with a loss that can be infinite. Moreover, \mathcal{L} is discontinuous in θ and has zero gradients almost everywhere, as the observed loss values only change in the proximity of the surface of the bounded region and are constant everywhere else. While \mathcal{L} is required to ensure conservativeness, its optimization is infeasible for the aforementioned reasons.

We hence employ two modifications to \mathcal{L} in order to make it usable in practice. First, we suggest to replace the fixed constants

Algorithm 1 Conservative loss. f is assumed to distribute over arrays like ξ .

```

1: procedure Loss( $\theta$ )
2:    $\mathbf{r} = \text{UNIFORM}()$ 
3:    $\xi = \text{SAMPLEREGION}(g, \mathbf{r})$ 
4:    $y = \text{ANY}(f(\xi))$ 
5:    $\hat{y} = h_\theta(\mathbf{x})$ 
6:   return  $-\alpha \cdot y \cdot \text{LOG}(\hat{y}) - \beta \cdot (1 - y) \cdot \text{LOG}(1 - \hat{y})$ 
7: end procedure

```

α and β with variable values $\alpha(t)$ and $\beta(t)$ that depend on the learning iteration (for details, see Suppl. Sec. 2.1). This ensures that, in the limit, the cost of FNs is unbounded, so the solution will eventually become conservative. Second, in order to compute smooth gradients for our neural bounding network h_θ , we approximate the previous \mathcal{L} via a variant of a weighted binary cross-entropy $\hat{\mathcal{L}}$:

$$\hat{\mathcal{L}}(\theta) = -\mathbb{E}_i[\alpha(t) \cdot y_i \log(\hat{y}_{i,\theta}) + \beta(t) \cdot (1 - y_i) \log(1 - \hat{y}_{i,\theta})], \quad (1)$$

where $\hat{y}_\theta = h_\theta(\mathbf{x})$ is the bounding network prediction with the current parameters θ for the current input \mathbf{x} , and the supervisory signal $y = f(\mathbf{x})$ is the result of evaluating the indicator f at the same location. The pseudocode for our loss is shown in Alg. 1.

3.2 Neural Bounding Hierarchies

We can also stack our neural bounding volumes into hierarchies, similar to how classic bounding boxes are used to compute a bounding volume hierarchy (BVH), with the added benefit that our neural hierarchy’s higher levels are again tightly and conservatively bounding the inner levels. Please note that while the NNs bound each node, the tree’s structure needs to be supplied by the user.

3.3 Neural Early-out

One advantage of bounding hierarchies is that testing can be interrupted early under some conditions, saving computation time. However, a typical NN can only be executed to the end to produce a result. We will next demonstrate we can also adapt our neural bounding approach to enable early-out as follows.

The idea is to use additional conservative and negated intermediate losses instead of a single conservative loss on the end. Consider the example of an MLP with two layers, A_1 and A_2 , and a non-linearity n1 , performing a conservative inside-test. The common loss, for simplicity at a single point, is

$$\mathcal{L}_{\text{Late}}(\mathbf{r}) = \text{bce}(h_\theta^{\text{Late}}(\mathbf{r}), g(\mathbf{r})), \quad \text{where} \quad (2)$$

$$h_\theta^{\text{Late}}(\mathbf{r}) = \text{n1}(A_2 \times (\text{n1}(A_1 \times (\mathbf{r}|1))|1)), \quad (3)$$

with bce denoting the binary cross-entropy and $(\cdot|1)$ the bias-trick. We instead train the loss

$$\mathcal{L}_{\text{Early}}(\mathbf{r}) = \mathcal{L}_{\text{Late}}(\mathbf{r}) + \text{bce}(h_\theta^{\text{Early}}(\mathbf{r}), 1 - g(\mathbf{r})), \quad \text{where} \quad (4)$$

$$h_\theta^{\text{Early}}(\mathbf{r}) = \text{n1}(A_3 \times (\mathbf{r}|1)), \quad (5)$$

with A_3 being a third layer of suitable size. Doing so, the network has to produce two conservative results at the same time: the final one, as well as an early one, that is the opposite of the first one. The final one requires executing a long network. The early one is typically a much simpler network. At test time, the early network is

executed first. If its output is negative, we can be certain no further testing is required and exit. If it is positive, the second network also gets executed to get the final answer. This is possible as the early-out is inverse conservative, enabled by our approach.

This concept can further be cascaded to include multiple intermediate exit points. It starts to be most effective if the NN gets complex. Our results show it to be around 25 % faster than a naive NN across a substantial range of tasks and dimensions and about twice as fast on the important case of point queries.

3.4 Implementation

While our approach is realized as a neural field, making it generally applicable and independent of any specific architecture, we have observed that certain architectural decisions impact the tightness of the bounding. We detail these choices in the following sections.

Architecture. In all cases, the input to our algorithm is the indicator function to be bounded, which is then sampled at m -dimensional query locations that are used to fit the network with our asymmetrical loss from Alg. 1. The output of the network is a floating point number that represents occupancy, restricted to $(0,1)$ via a Sigmoid and then rounded to $\{0,1\}$. For our concrete implementation, our network is implemented as MLP in order to deal with arbitrary-dimensional queries. The architecture details for all results shown in this paper are reported in Suppl. Tab. 3. Sinusoidal activations are used in the hidden layers, and the output layer is activated by a Sigmoid function. We have experimented with both residual- and skip-connections [He et al. 2016; Ronneberger et al. 2015] as well as Batch-Normalization [Ioffe and Szegedy 2015], but found little improvement, presumably due to the shallow network depth. For some results, we use positional encodings (see Suppl. Sec. 3).

Training. We build and train our networks in PyTorch [Paszke et al. 2019] and use the standard layer initialization, which we have found to especially perform favorably in higher dimensions. We use the Adam optimizer [Kingma and Ba 2014] with a learning rate of 1×10^{-3} and implement $\alpha(t)$ and $\beta(t)$ as a linear step-wise schedule that is incremented every 10,000 training iterations (see Suppl. Sec. 2.1 for details). We use a batch size of 200,000 and early-stop the training as soon as FN = 0 is reached and has been stable for the past six scheduling iterations. Depending on dimensionality and query complexity, this typically takes between 20 to 60 minutes on a modern workstation.

Please note that the concept of “epochs” or train/test splits applies differently to generalization across a continuous space: For learning and validation, we randomly sample this space, and for testing we do the same. Our proposed method does not aim to learn generalization across objects, but a generalization of bounds across the hypercube of space, time, query type, and combinations thereof. We would like to emphasize that this is the same task which classic bounding geometry performs, where a bounding box would also not generalize from a bunny to, e.g., a dragon.

4 EVALUATION

The analysis of our results is structured around studying different bounding methods (e.g., boxes, spheres, k -DOPs, etc., see Sec. 4.1)

on different tasks, which we define as different query types in varying dimension (Sec. 4.2).

4.1 Methods

We evaluate our approach’s performance against different classic bounding primitives. First, we compare to axis-aligned and non-axis-aligned (oriented) bounding boxes (**AABBox** and **OBox**), followed by bounding by a **Sphere** and its anisotropically scaled counterparts, axis-aligned and oriented ellipsoids (**AAEllipsoid** and **OEllipsoid**), respectively, which all can be fit in closed form [Schneider and Eberly 2002]. Another widely-used bounding method we consider is k -DOPs, method **kDOP**, implemented following Ericson [2004]. We set k , the number of planes, to $4m$, scaling with the dimensionality.

BVH are a method common for spatial queries in graphics with the benefit of early interruption and not having to compare every node in the hierarchy to a query. Hence, we include a baseline, using a linear builder [Lauterbach et al. 2009] with Morton-order and median splits. Queries are processed in batches with persistent work queues [Aila and Laine 2009]. Note that we use the BVH to perform bounding queries, also when applied to rays, and not to trace rays, i.e., find the nearest hit position.

OurNN and **OurNNEarly** implement our neural bounding method, without and with early-out, respectively, as detailed in Sec. 3.4.

To demonstrate our method is not limited to classic neural fields, we include a neural grid method [Karnewar et al. 2022], called **OurReLUField**, which does not scale to high dimensions, but is extremely fast to train.

Finally, the application of our proposed asymmetric loss is not restricted to neural networks, but can also be applied to other optimization problems. We therefore explore replacing our network with a set of k -DOP planes which are then optimized with our asymmetric loss. We call this method **OurkDOP**, which has the speed and memory usage of traditional k -DOPs but benefits from parameters found by modern gradient descent.

To verify the contribution of our asymmetric training loss, we study a variant of our approach that uses a symmetric loss which weights both FPs and FNs with the same weight, i.e., $\alpha = \beta = 1$. Due to its similarity to the classic occupancy networks [Mescheder et al. 2019], we call this method **OccNet**. Please note that **OccNet** is not a method that can be deployed for bounding in practical scenarios, as it does not produce conservative results (i.e., the false-negative rate is not zero). We would like to re-emphasize that deploying non-conservative bounding method in graphics would lead to missing geometry, i.e., rays that do actually intersect a 3D object will wrongly test negative (see column **OccNet** in Fig. 10). We hence only show qualitative, not quantitative results of this method.

Because of numerics, it is typical that our and other methods designed to be conservative on an (infinite) training sample set might be non-conservative on a hidden test set. Consider fitting a single plane to classify space in two: the exact plane equation might not be float-representable. The same is true for the parameters of a NN which are also floating-point. To account for this at finite training time, we add an epsilon (see supplemental) to each methods’ output. With our methods, we find fewer than 1 FN in 100 million queries on hidden test sets, and this will decrease with more training.

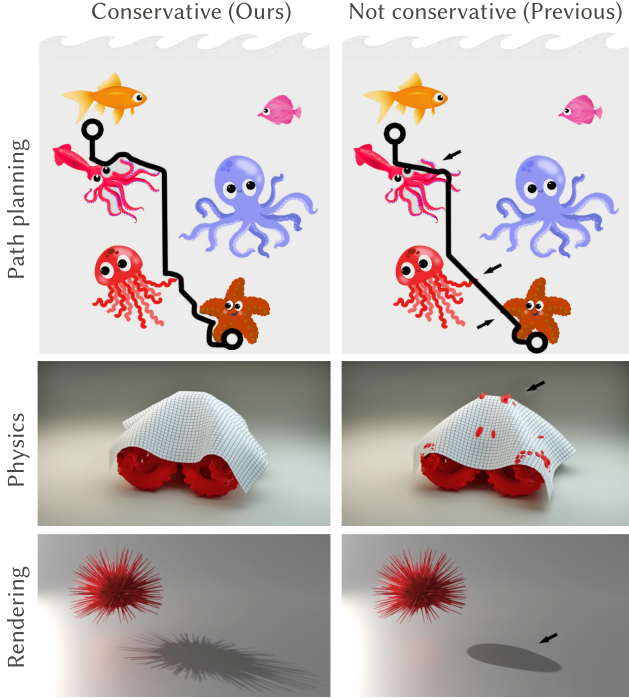


Figure 2: Motivating examples for conservative queries: we encode the world as a NN trained with (left) and without (right) our proposed approach. When used for 2D path-planning, our representation achieves a collision-free trajectory (left), whereas the non-conservative NN collides (arrows). Similar observations can be made when using the NN as a proxy for 3D cloth collision leading to erroneous interpenetration in the middle row, or as a proxy to cull shadow rays where the stings are missing in the shadow.

4.2 Tasks

In this analysis, a “task” combines two properties: the dimension of the indicator function (we study $n = 2, 3$ and 4) and the type of query (points, rays, planes and boxes), which builds up to eight-dimensional problems. Fig. 2 shows some examples of these queries.

Indicators. For 2D data we use images of single natural objects in front of a white background where the alpha channel defines the indicator function. We use 9 such images. For 3D data, we use 9 voxelized shapes of popular test meshes, such as the Stanford Bunny and the Utah teapot. We show these objects in Suppl. Fig. 1. For 4D data, we study sets of animated objects: we load random shapes from our 3D data and create time-varying occupancy data by rotating them around their center. We obtained 3 samples of this distribution and would like to emphasize that this is a strategy that favors the baselines: if object transformations were characterized by translational instead of rotational motions, the performance of the baseline approaches would deteriorate significantly. **AABox**, for instance, would have to bound the entire spatial extent between the initial and terminal object locations, thereby yielding an exceedingly high number of false-positive intersections.

Query types. Our query types are point-, ray-, plane- and box-queries. For all query types, the goal is to ask, given a point, ray, plane or box, does it intersect the object to be bounded? Rays are parameterized as origin and direction vector, planes as normal and point p_0 on the plane surface, and boxes by their minimum and maximum corners. For every query region, the result is computed as $\text{any}()$ of a sample of the indicator across the region.

4.3 Metrics

We report results for the two relevant metrics which define the quality of a bounding approach: *tightness* and *execution speed*.

Tightness. In terms of tightness, FP is the only figure of merit to study, as a high FP rate will result in many unnecessary intersection tests. This is worsened if not working with hierarchies (or on their lowest level), as then every FP leads to an expensive test against the entire bounded geometry, with often millions of triangles. We compute the FP and FN using MC of one million values.

Although our task is (space) classification, we do not employ classic metrics such as F1, precision and recall, as these capture the relation between FPs and FNs, which in our case is not relevant, since the FN rate for all bounding methods must be strictly zero.

Speed. This is the speed of the bounding operation itself (e.g., evaluating the closed-form sphere intersection, or, for method **OurNN**, a network forward pass). We report both query speed and ray throughput as the average number over 10,000 independent runs with 10 million randomly sampled, forward-facing 3D rays. For fairness, our methods and all baselines have been implemented as vectorized PyTorch code and make full use of GPU acceleration.

4.4 Results

Quality. We show our quantitative results and the comparisons against the baselines in Tbl. 1. As is evident, our method **OurNN** consistently outperforms the other baselines by a large margin (up to $8\times$ improvement on 4D point queries). **BVH** performs second best across the tasks, roughly trailing ours by three or four times more FPs. The follow-up methods are on average **kDOP** and **OurkDOP**. Interestingly, using modern gradient-descent based construction for **OurkDOP** improves on **kDOP** results significantly. Unsurprisingly, all methods increase their FP rate when going to higher dimension, a testimony to the increased query complexity. Notably, our method scales favorably with dimension and achieves acceptable FP rates even at high dimensions (e.g., for 4D box queries). Moreover, especially in higher dimensions (e.g., 4D ray, plane, box), the baselines approach uniform performance, e.g., **AABox** vs **kDOP**, differing by only a few percentage points. **BVH** does better here, getting closer to our performance, but still with a margin. The relation of our variant **OurNNEarly** to **OurNN** is favorable: early-out creates slightly more FP in some cases, but the gain is the win in test compute time studied later. The other variant **OurReLUField** is performing worst



Figure 3: Result for **OurkDOP.** Image credit: 588ku, PNGTree.com

of all neural methods, trains and tests extremely fast. Fig. 6 visualizes the same data in the form of a rank plot, see figure caption for discussion. Qualitative results for 2D and 3D are shown and discussed in Fig. 1 and Fig. 10, respectively.

In Fig. 3 we show result for **OurKDOP** at $k = 6$, where the planes were found via stochastic gradient descent and our loss.

Ours performs better than the common heuristics [Ericson 2004]. This indicates that our approach to finding bounding parameters can be superior to heuristics, even if the model itself is not neural.

We further show a result for an interesting variant of our method, that does not conservatively state which spatial location might be hit, but conservatively bounds which spatial locations certainly are hit. This is achieved by flipping the asymmetry-weights α and β . An example is seen in Fig. 4 for 2D and Fig. 9 for 3D. This is useful for a quick broad-phase test in collision: an object only needs to be tested if it is neither certainly out nor certainly-in. Fig. 11 shows our **OurNN** for NNs of different complexity. Fig. 5 shows a bounding hierarchy on a school of 2D fish.

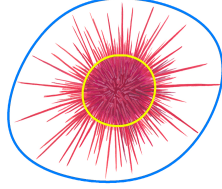


Figure 4: Conservative bounding of never- (blue) and always-hit (yellow).

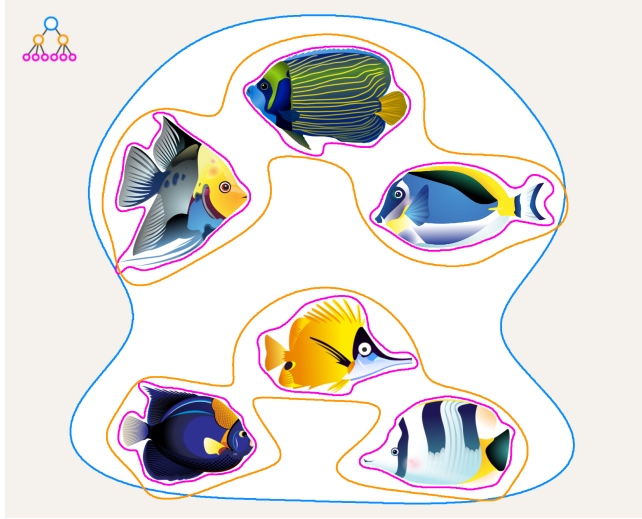


Figure 5: A hierarchy of neural bounding networks. The first level is show in blue, the two child nodes in yellow and the leafs in pink. Note that it is not required for the higher-level bounding to bound the lower-level bounding. It is only required to bound the indicator.

Speed. We quantify the speed of our bounding operations in Tbl. 2. While we obviously cannot match the speed of simpler bounding methods such as **Sphere** or **AABBox**, we were surprised to find that our implementation of our neural bounding queries is not much slower than **kDOP** and some of the oriented bounding methods. Therefore, even if we nominally lag behind in this comparison

(by a factor of min. 1.1 \times , **OurNNEarly** vs **kDOP**, and max. 19.6 \times , **OurNNEarly** vs. **Sphere**), we would argue that this is offset by the substantial reduction in FP (on average $\times 12$, see Tbl. 1 and Sec. 5).

5 DISCUSSION

Can a network that is slower than traditional bounding primitives be useful in practical graphics problems? There are two supportive arguments we will discuss in the following: tightness and scalability.

Tightness. In order to evaluate the speed of a bounding method, one must additionally take into account the cost of a false-positive query, i.e., having to perform an intersection against the detailed, bounded geometry. Assume a bounding method B can be queried in time t_b , and the competing bounding method A is five times slower, i.e., $t_a = 5 t_b$. Assume further that A, in spite of being slower, produces significantly fewer false-positives ($p_a = 0.1$) than B ($p_b = 0.3$). Finally, assume that performing tests with the actual detailed geometry needs time t , which is usually much larger than t_a and t_b . The total time for N tests, regardless of the method used, then is $N t_i + p_i \cdot N \cdot t$, of which the first term marks indispensable checks (as every ray must be checked against the bounding method), and the second term marks unnecessary checks due to false-positive bounding queries. For method A to win, the following must hold:

$$N \cdot t_a + N p_a \cdot t < N \cdot t_b + N p_b \cdot t$$

$$t_a + p_a \cdot t < t_b + p_b \cdot t$$

$$t_a + p_a \cdot t - p_b \cdot t < t_b$$

$$p_a \cdot t - p_b \cdot t < t_b - t_a$$

$$t(p_a - p_b) < t_b - t_a$$

$$\text{and hence if } (p_a - p_b) > 0 : t < (t_b - t_a) / (p_a - p_b)$$

$$\text{or otherwise if } (p_a - p_b) < 0 : t > (t_b - t_a) / (p_a - p_b). \quad (6)$$

For the aforementioned example values, this produces

$$t > (t_b - 5 t_b) / (0.1 - 0.3) = 20 t_b,$$

which means that method A is to be preferred if tests against the actual bounded geometry are at least 20 times as expensive as the bounding query. As traditional triangle meshes often have millions of triangles, this is easily achieved by our approach.

We quantify the factor by which a 3D ray-geometry test has to be more expensive than the bounding test in the right column of Tbl. 2 and see that our method is to be preferred when the geometry test is as little as 9 \times more expensive (for **kDOP**, avg. over all methods is 70.2), which certainly is achieved in most real-world applications.

Early-out. In

Fig. 7 we analyze the effectiveness of **OurNNEarly**, relative to **OurNN** in more detail. The plot shows the ratio of both method's runtime, across all our tasks and dimensions, sorted from low to high. There are four cases, mostly plane-type, where the speed gain is marginally below

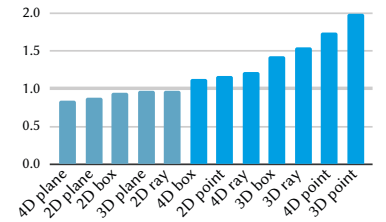


Figure 7: Early-out speed (see text).

Table 1: False-positive rates for different bounding methods (rows) in different dimensions (columns) on different query types (subcolumns). Lower means better, means fewer unnecessary tests. The best result per dimension and task is shown in bold.
¹(Grids, like **OurReLUField** do not scale to higher dimensions.)

| | 2D | | | | 3D | | | | 4D | | | |
|---------------------|-------------|-------------|-------------|-------------|-------------|----------------|----------------|----------------|--------------|----------------|----------------|----------------|
| | Point | Ray | Plane | Box | Point | Ray | Plane | Box | Point | Ray | Plane | Box |
| AABox | 28.4% | 43.9% | 21.3% | 11.0% | 28.5% | 69.3% | 19.1% | 18.9% | 81.7% | 70.3% | 3.6% | 38.0% |
| OBox | 27.0% | 29.3% | 21.2% | 21.9% | 26.1% | 52.5% | 19.1% | 36.4% | 76.2% | 68.9% | 3.6% | 37.7% |
| Sphere | 40.2% | 43.9% | 21.3% | 27.3% | 56.7% | 69.3% | 19.1% | 47.3% | 84.5% | 70.4% | 3.6% | 40.6% |
| AAEllli | 39.6% | 43.9% | 21.3% | 26.9% | 52.2% | 69.3% | 19.1% | 45.1% | 82.8% | 70.4% | 3.6% | 40.5% |
| OElli | 28.8% | 36.2% | 21.3% | 23.3% | 29.1% | 62.9% | 19.1% | 37.1% | 74.2% | 68.8% | 3.6% | 39.9% |
| kDOP | 28.4% | 33.4% | 21.2% | 8.9% | 22.0% | 65.6% | 19.1% | 17.4% | 75.3% | 70.0% | 3.6% | 36.4% |
| BVH | 10.4% | 28.9% | 15.3% | 8.2% | 10.0% | 34.4% | 18.4% | 14.6% | 39.8% | 61.7% | 3.6% | 35.2% |
| OurkDOP | 19.5% | 18.5% | 14.3% | 7.7% | 15.1% | 40.0% | 18.0% | 15.3% | 62.0% | 64.7% | 3.6% | 31.6% |
| OurReLUField | 5.0% | 6.4% | 5.7% | 3.3% | 3.3% | — ¹ | — ¹ | — ¹ | 10.0% | — ¹ | — ¹ | — ¹ |
| OurNN | 3.2% | 2.7% | 1.2% | 2.2% | 4.2% | 7.6% | 5.6% | 5.0% | 10.9% | 31.0% | 3.1% | 11.3% |
| OurNNEarly | 2.8% | 3.3% | 1.3% | 3.1% | 2.9% | 10.1% | 5.7% | 6.5% | 11.5% | 38.8% | 3.1% | 17.2% |

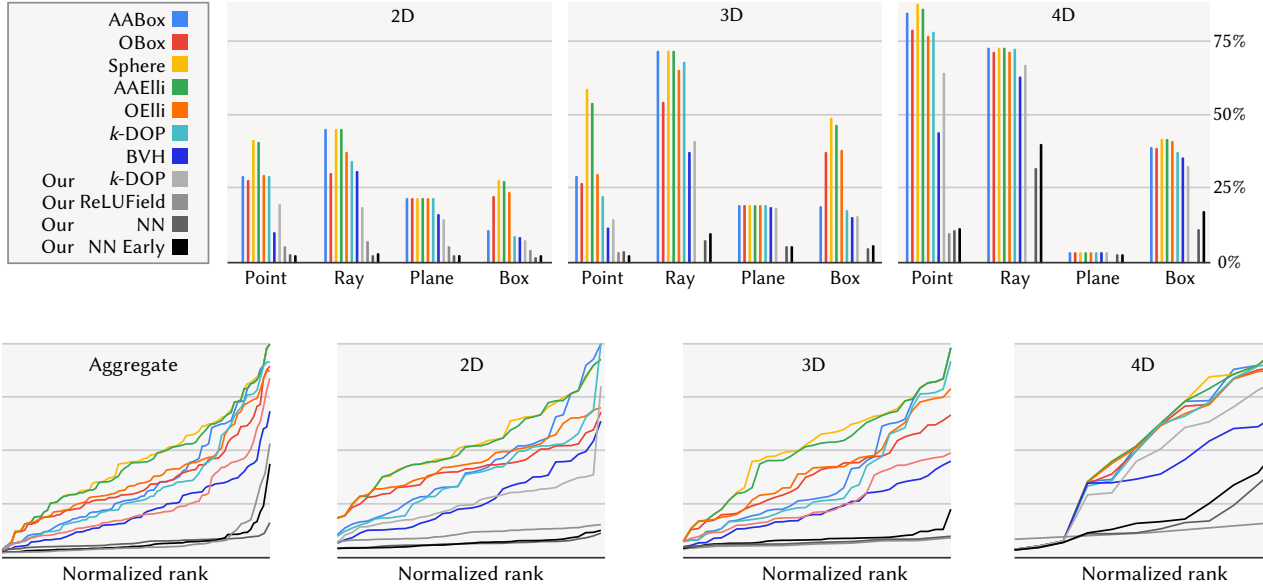


Figure 6: FP rates (vertical axis) for each test object, sorted in ascending order (horizontal axis). We show all methods (colored lines) across all dimensions (horizontal subplots). While Tbl. 1 reports average performance, this graphical representation reveals that our method **OurNN, despite having a few higher negative examples, consistently yields the lowest FP rates across all categories. The average of **OurkDOP** and **OurNNEarly** seem affected by some hard cases.**

one. Otherwise, it is positive, including the most important case of 3D point queries being twice as fast. The mean gain is 24.3 %.

Convergence. In Fig. 8, we analyze the convergence for two scenes. Each plot horizontally shows iterations and loss vertically. Our method is shown in blue, the common loss in red. FN in solid, FP in dotted.

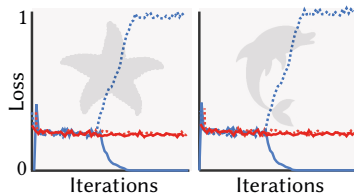


Figure 8: Convergence (see text).

We see that ours, when the loss is ramped, reduces the FN to zero, at the expense of growing FPs. Fig. 13 shows that our approach can equally well be applied to non-MLP architectures. Overall, our method incurs a training overhead. Representations that train slowly remain slow, but if training is fast, it remains fast with our method (see Fig. 13).

Scalability. To demonstrate scalability to complex high-dimensional spaces, we finally bound an entire generative model itself in Fig. 12. We use a pre-trained variational auto-encoder (VAE) of MNIST digits as the indicator. This is a 12-dimensional space of 10 VAE latent dimensions and the 2D pixel coordinate. Note that a pre-trained VAE is a deterministic 12-D indicator function,

Table 2: Speed and throughput of different methods. Throughput is in billions of rays per second. The rightmost column shows the factor by which a geometry test has to be more expensive than querying the bounding method for our method (with early-out) to pay off, as per Eq. 6.

| | Speed (ms) | Throughput | Ratio |
|------------|------------|------------|--------|
| AABox | 2.58 | 3.88 | 78.78 |
| OBox | 2.58 | 3.88 | 103.08 |
| Sphere | 2.36 | 4.24 | 74.15 |
| AAElli | 2.39 | 4.19 | 74.10 |
| Oelli | 2.39 | 4.18 | 83.07 |
| kDOP | 41.27 | 0.24 | 9.06 |
| BVH | 25.67 | 0.39 | 84.82 |
| OurkDOP | 11.84 | 0.84 | 114.92 |
| OurNN | 70.82 | 0.14 | — |
| OurNNEarly | 46.30 | 0.22 | — |

independent of the question of whether it was trained non-deterministically. This allows to predict which pixels will belong to a digit without even running the generative model. While this is a toy problem, in more engineered applications it would, e.g., allow conservative ray intersection with complex 3D models that have not even yet been generated.

Limitations. However, our approach also comes with certain limitations, which we will highlight here to inspire future work:

Foremost, our method neither provides an algorithmic guarantee to have no FNs, nor is it a new bounding primitive. Instead, we heuristically incentivize conservativeness via our proposed loss (Eq. 1). Future investigations will have to explore algorithmic conservativeness and other forms of hard constraints in NN training.

Our method does not generalize across objects, but –as is common for neural fields– is trained per-object. The training takes significantly longer than inferring traditional bounding primitives, many of which have closed-form solutions, which has practical implications for animated scenes. While this can easily be outsourced to a pre-processing stage, there is potential in maximizing training speed by either incorporating the fully-fused NN architecture proposed by [Müller et al. 2022] or by meta-learning [Fischer and Ritschel 2022; Sitzmann et al. 2020; Tancik et al. 2021] a space of bounding networks, which would be especially useful for bounding similar geometry that only slightly differs in shape or pose.

Furthermore, our method’s intersection speed is not yet competitive with methods from 3D ray tracing, which benefit from years of optimization research, such as ray-box or BVH intersections.

Additionally, sampling the indicator only works if object- and query-dimensions align. An example is sampling points in 2D space but testing against a 1D line, which will not work, as the probability of sampling a point on the line is zero. This can be alleviated by re-parameterizing the sampler to sample directly on the line instead.

Finally, as we overfit a network per shape, our approach requires additional storage in the order of magnitude of the network parameters (e.g., 2,801 parameters for a 3D point query network), which naturally is larger than for traditional baselines (see Tbl. 2). However, storage is cheaper than compute, and moreover, applications

which use bounding geometry usually handle large meshes with many triangles, leading us to believe that our modest storage requirement for the network parameters is negligible in comparison.

6 CONCLUSION

In future work, the idea of asymmetric losses might be applicable to other neural primitives like hashing. In a similar vein, distance fields could be trained to maybe underestimate, but never overestimate distance so as to aid sphere tracing. It is further conceivable to bound not only geometry but also other quantities like radiance fields or their statistics for image synthesis.

Our results are only almost always conservative, as they involve two stages of sampling, that, in expectation, will be conservative, but we lack any proof under what conditions the probability of being truly conservative is how high. The step of sampling the query region could be replaced by an unbiased (and potentially closed-form) one; we only choose sampling here as it works on any indicator in any dimension. However, the loss is still an empirical loss, and there is a nonzero chance that a tiny part of the indicator would remain unattended with finitely many samples. In practice, our results show dozens of tasks with many instances, each tested with hundred-thousands of samples with no FN result.

Using our technique, bounding in graphics can benefit from many of the exciting recent innovations around NNs such as improved architectures, advanced training, or dedicated neural hardware.

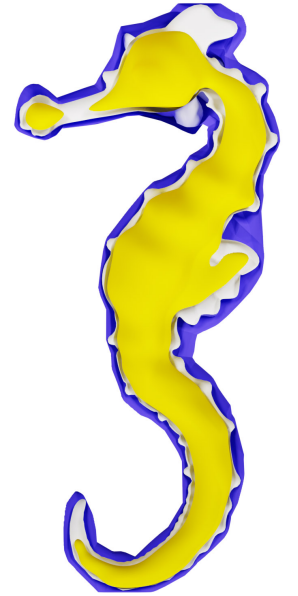


Figure 9: 3D-bounding no-hit (blue) and hit (yellow).

REFERENCES

- Timo Aila and Samuli Laine. 2009. Understanding the efficiency of ray traversal on GPUs. In *Proceedings of the conference on high performance graphics 2009*. 145–149.
- Matan Atzmon and Yaron Lipman. 2020. Sal: Sign agnostic learning of shapes from raw data. In *CVPR*. 2565–2574.
- Annada Prasad Behera and Subhankar Mishra. 2023. Neural directional distance field object representation for uni-directional path-traced rendering. *arXiv preprint arXiv:2306.16142* (2023).
- Gino van den Bergen. 1997. Efficient collision detection of complex deformable models using AABB trees. *J Graphics Tools* 2, 4 (1997), 1–13.
- Xinhao Cai, Eulalie Coevoet, Alec Jacobson, and Paul Kry. 2022. Active Learning Neural C-space Signed Distance Fields for Reduced Deformable Self-Collision. In *Graphics Interface*.
- Edward R Dougherty. 1992. An introduction to morphological image processing. In *SPIE*.
- Stephen A Ehmman and Ming C Lin. 2001. Accurate and fast proximity queries between polyhedra using convex surface decomposition. *Comp Graph Forum* 20, 3 (2001), 500–511.
- Christer Ericson. 2004. *Real-time collision detection*. Crc Press.

- Michael Fischer and Tobias Ritschel. 2022. Metappearance: Meta-learning for visual appearance reproduction. *ACM Trans Graph (Proc. SIGGRAPH)* 41, 6 (2022), 1–13.
- Shin Fujieda, Chih-Chen Kao, and Takahiro Harada. 2023. Neural Intersection Function. *arXiv preprint arXiv:2306.07191* (2023).
- Yan Gu, Yong He, Kayvon Fatahalian, and Guy Blöchl. 2013. Efficient BVH construction via approximate agglomerative clustering. In *Proc. HPG*. 81–88.
- Johannes Günther, Stefan Popov, Hans-Peter Seidel, and Philipp Slusallek. 2007. Real-time ray tracing on GPU with BVH-based packet traversal. In *Symp Interactive Ray Tracing*. 113–118.
- Koji Hashimoto, Tomoya Naito, and Hisashi Naito. 2023. Neural Polytopes. *arXiv preprint arXiv:2307.00721* (2023).
- Kaiming He, Xiangyu Zhang, Shaoqing Ren, and Jian Sun. 2016. Deep residual learning for image recognition. In *CVPR*. 770–778.
- Sergey Ioffe and Christian Szegedy. 2015. Batch normalization: Accelerating deep network training by reducing internal covariate shift. In *ICCV*. 448–456.
- Animesh Karnewar, Tobias Ritschel, Oliver Wang, and Niloy Mitra. 2022. ReLU fields: The little non-linearity that could. In *ACM SIGGRAPH*. 1–9.
- Timothy L Kay and James T Kajiya. 1986. Ray tracing complex scenes. *ACM SIGGRAPH Computer Graphics* 20, 4 (1986), 269–278.
- Diederik P Kingma and Jimmy Ba. 2014. Adam: A method for stochastic optimization. *arXiv preprint arXiv:1412.6980* (2014).
- James T Klosowski, Martin Held, Joseph SB Mitchell, Henry Sowizral, and Karel Zikan. 1998. Efficient collision detection using bounding volume hierarchies of k -DOPs. *IEEE TVCG* 4, 1 (1998), 21–36.
- Christian Lauterbach, Michael Garland, Shubhabrata Sengupta, David Luebke, and Dinesh Manocha. 2009. Fast BVH construction on GPUs. In *Computer Graphics Forum*, Vol. 28. Wiley Online Library, 375–384.
- Chen Liu, Michael Fischer, and Tobias Ritschel. 2023. Learning to learn and sample BRDFs. *Comp Graph Forum (Proc. Eurographics)* 42, 2 (2023), 201–211.
- Daniel Meister, Shinji Ogaki, Carsten Benthin, Michael J Doyle, Michael Guthe, and Jiri Bittner. 2021. A survey on bounding volume hierarchies for ray tracing. *Comp Graph Forum* 40, 2 (2021), 683–712.
- Lars Mescheder, Michael Oechsle, Michael Niemeyer, Sebastian Nowozin, and Andreas Geiger. 2019. Occupancy Networks: Learning 3D Reconstruction in Function Space. In *CVPR*.
- Thomas Müller, Alex Evans, Christoph Schied, and Alexander Keller. 2022. Instant neural graphics primitives with a multiresolution hash encoding. *ACM Trans Graph (Proc. SIGGRAPH)* 41, 4 (2022), 1–15.
- Ntumba Elie Nsambi, Adarsh Djeacoumar, Hans-Peter Seidel, Tobias Ritschel, and Thomas Leimkühler. 2023. Neural Field Convolutions by Repeated Differentiation. *arXiv preprint arXiv:2304.01834* (2023).
- Jeong Joon Park, Peter Florence, Julian Straub, Richard Newcombe, and Steven Lovegrove. 2019. DeepSDF: Learning Continuous Signed Distance Functions for Shape Representation. In *CVPR*.
- Adam Paszke, Sam Gross, Francisco Massa, Adam Lerer, James Bradbury, Gregory Chanan, Trevor Killeen, Zeming Lin, Natalia Gimelshein, Luca Antiga, et al. 2019. Pytorch: An imperative style, high-performance deep learning library. *NeurIPS* 32 (2019).
- Christian Reiser, Songyou Peng, Yiyi Liao, and Andreas Geiger. 2021. Kilonerf: Speeding up neural radiance fields with thousands of tiny MLPs. In *ICCV*. 14335–14345.
- Tal Ridnik, Emanuel Ben-Baruch, Nadav Zamir, Asaf Noy, Itamar Friedman, Matan Protter, and Lihi Zelnik-Manor. 2021. Asymmetric loss for multi-label classification. In *ICCV*. 82–91.
- Olaf Ronneberger, Philipp Fischer, and Thomas Brox. 2015. U-net: Convolutional networks for biomedical image segmentation. In *Proc. MICCAI*. 234–241.
- Igor Santesteban, Miguel Otaduy, Nils Thuerey, and Dan Casas. 2022. Ulnet: Untangled layered neural fields for mix-and-match virtual try-on. *NeurIPS* 35 (2022), 12110–12125.
- Philip Schneider and David H Eberly. 2002. *Geometric tools for computer graphics*. Elsevier.
- Nicholas Sharp and Alec Jacobson. 2022. Spelunking the deep: Guaranteed queries on general neural implicit surfaces via range analysis. *ACM Trans Graph (Proc. SIGGRAPH)* 41, 4 (2022), 1–16.
- Vincent Sitzmann, Eric Chan, Richard Tucker, Noah Snavely, and Gordon Wetzstein. 2020. MetaSDF: Meta-learning signed distance functions. *NeurIPS* 33 (2020), 10136–10147.
- Matthew Tancik, Ben Mildenhall, Terrance Wang, Divi Schmidt, Pratul P Srinivasan, Jonathan T Barron, and Ren Ng. 2021. Learned initializations for optimizing coordinate-based neural representations. In *CVPR*. 2846–2855.
- Thijs Vogels, Fabrice Rousselle, Brian McWilliams, Gerhard Rothlin, Alex Harvill, David Adler, Mark Meyer, and Jan Novák. 2018. Denoising with kernel prediction and asymmetric loss functions. *ACM Trans Graph (Proc. SIGGRAPH)* 37, 4 (2018), 1–15.
- René Weller, David Mainzer, Abhishek Srinivas, Matthias Teschner, and Gabriel Zachmann. 2014. Massively Parallel Batch Neural Gas for Bounding Volume Hierarchy Construction. In *VRIPHYS*. 9–17.
- Yiheng Xie, Towaki Takikawa, Shunsuke Saito, Or Litany, Shiqin Yan, Numair Khan, Federico Tombari, James Tompkin, Vincent Sitzmann, and Srinath Sridhar. 2022. Neural Fields in Visual Computing and Beyond. *Comp Graph Forum* 41, 2 (2022).
- Lior Yariv, Jiatao Gu, Yoni Kasten, and Yaron Lipman. 2021. Volume rendering of neural implicit surfaces. *NeurIPS* 34 (2021), 4805–4815.
- Ryan S Zesch, Bethany R Witemeyer, Ziyan Xiong, David IW Levin, and Shinjiro Sueda. 2022. Neural collision detection for deformable objects. *arXiv preprint arXiv:2202.02309* (2022).
- Xiong Zhou, Xianming Liu, Junjun Jiang, Xin Gao, and Xiangyang Ji. 2021. Asymmetric loss functions for learning with noisy labels. In *ICML*. 12846–12856.
- Charu C. Aggarwal, Alexander Hinneburg, and Daniel A. Keim. 2001. On the surprising behavior of distance metrics in high dimensional space. In *Database Theory*. 420–434.
- Angel X. Chang, Thomas Funkhouser, Leonidas Guibas, Pat Hanrahan, Qixing Huang, Zimo Li, Silvio Savarese, Manolis Savva, Shuran Song, Hao Su, Jianxiong Xiao, Li Yi, and Fisher Yu. 2015. ShapeNet: An Information-Rich 3D Model Repository. Technical Report arXiv:1512.03012 [cs.GR], Stanford University – Princeton University – Toyota Technological Institute at Chicago.
- Ben Mildenhall, Pratul P. Srinivasan, Matthew Tancik, Jonathan T. Barron, Ravi Ramamoorthi, and Ren Ng. 2021. Nerf: Representing scenes as neural radiance fields for view synthesis. *Communications of the ACM* 65, 1 (2021), 99–106. ACM New York, NY, USA.

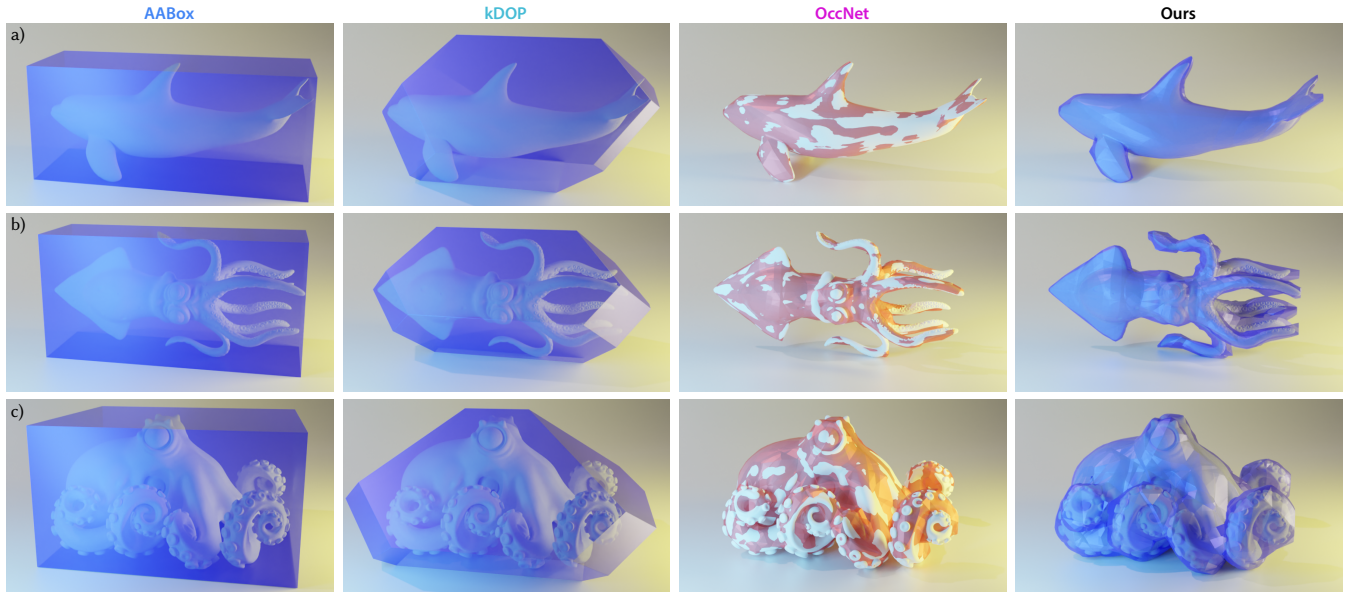


Figure 10: Comparison of methods (columns) for different 3D shapes (rows). **AABox** and **kDOP** both bound the objects conservatively, but create false positives, whereas **OccNet** bounds overtight and produces false negatives (red). Our approach is both tight and conservative.

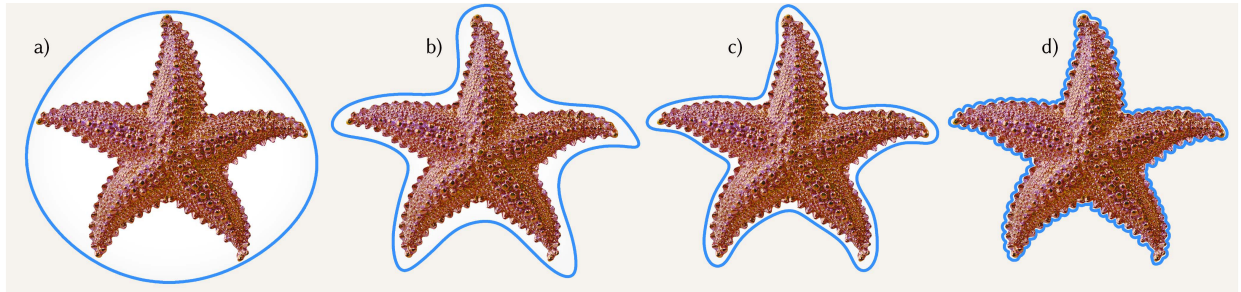


Figure 11: Our learned bounding volumes with increasingly complex neural networks from left to right. A simple network, left, fits the shape only roughly, but still conservative. With increasing expressiveness towards the right, the fit gets more accurate and recovers concave regions, and later, the curvature of the starfish's arms. For a complex NN it becomes almost pixel-exact, but even then, small approximation errors are made but never violating the bounding requirement (zero FN). This indicates we can achieve conservativeness independent of complexity.

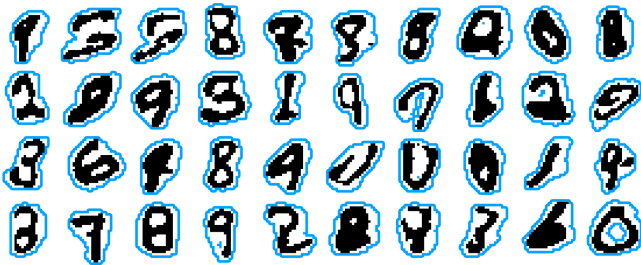


Figure 12: Results of applying our method to a VAE that generates MNIST digits, here shown for random latent codes. The blue borders are our bounds.

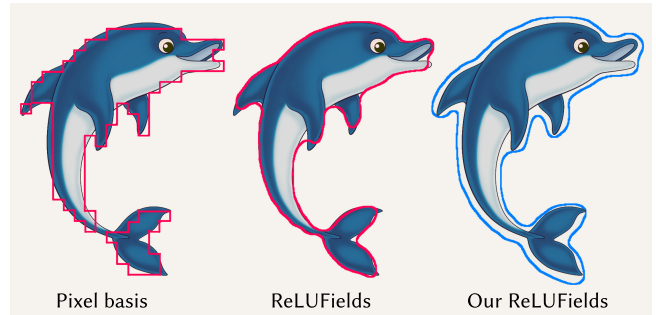


Figure 13: Application of our training to ReLUFields [Karnawar et al. 2022], an example of a fast-trainable architecture. Left shows a pixel basis result, middle a ReLUField of the same resolution and left our result.

Neural Bounding: Supplemental

Stephanie Wenxin Liu
Birkbeck, University of
London
United Kingdom
wenxin.liu.cs@gmail.com

Michael Fischer
University College London
United Kingdom
m.fischer@cs.ucl.ac.uk

Paul D. Yoo
Birkbeck, University of
London
United Kingdom
p.yoo@bbk.ac.uk

Tobias Ritschel
University College London
United Kingdom
t.ritschel@ucl.ac.uk

ACM Reference Format:

Stephanie Wenxin Liu, Michael Fischer, Paul D. Yoo, and Tobias Ritschel. 2024. Neural Bounding: Supplemental. In *Special Interest Group on Computer Graphics and Interactive Techniques Conference Papers '24 (SIGGRAPH Conference Papers '24)*, July 27-August 1, 2024, Denver, CO, USA. ACM, New York, NY, USA, 3 pages. <https://doi.org/10.1145/3641519.3657442>

1 INTRODUCTION

This document provides details on training used (Sec. 2), methods investigated (Sec. 3), data tested (Sec. 4), speed observed (Sec. 5) and an analysis of complexity (Sec. 6) of our method.

2 TRAINING

Our training uses a combination of scheduling the weights of different loss terms (Sec. 2.1) and regularization (Sec. 2.2).

2.1 Weight schedule

We provide more details on the $\alpha(t)$ and $\beta(t)$ schedules mentioned in the main document.

$\alpha(t)$ is a linear schedule that depends on the indicator dimension. For 2D, $\alpha(t)$ decreases by 1/20, 1/40, 1/60 etc.; for 3D, $\alpha(t)$ decreases by 1/100, 1/200, 1/300, etc.; for 4D, $\alpha(t)$ decreases by 1/200, 1/400, 1/600, etc., every 10,000 iterations if not 0 false-negatives (FNs). We observe that we need a greater degree of asymmetry to achieve conservativeness in higher dimensional space, because as the dimensionality increases, the number of samples required to adequately cover the space also increases. Therefore to effectively eliminate FNs in a greater number of samples requires a bigger degree of asymmetry.

$\beta(t)$ is a linear schedule that increases by 0.2 every 10,000 iterations if not 0 FNs. This is just a tweak in order to speed up training - decreasing $\alpha(t)$ alone already achieves conservativeness, as conservativeness only depends on the degree of asymmetry.

2.2 Regularization

We use L1 and L2 regularizations in our methods, lambda ranging from 0 to $5e-7$ increasing in a linear schedule.

Permission to make digital or hard copies of all or part of this work for personal or classroom use is granted without fee provided that copies are not made or distributed for profit or commercial advantage and that copies bear this notice and the full citation on the first page. Copyrights for components of this work owned by others than the author(s) must be honored. Abstracting with credit is permitted. To copy otherwise, or republish, to post on servers or to redistribute to lists, requires prior specific permission and/or a fee. Request permissions from permissions@acm.org.

SIGGRAPH Conference Papers '24, July 27-August 1, 2024, Denver, CO, USA

© 2024 Copyright held by the owner/author(s). Publication rights licensed to ACM.

ACM ISBN 979-8-4007-0525-0/24/07...\$15.00

<https://doi.org/10.1145/3641519.3657442>

3 METHODS

To make methods most comparable, we handle numerics fairly (Sec. 3.1) and use the same input parameterization (Sec. 3.2).

3.1 Numerics

An epsilon value of $1e-5$ is applied to the output of all methods to account for numerics.

3.2 Parameterization

We encode rays as pairs of Cartesian n D start- and direction-vectors; boxes as pairs of Cartesian n D corners and planes as n D p_0 and normal.

3.3 Our architecture

We detail the architectures used to produce the main paper figures in 5. “Main Tab. i ” refers to table i in the main document.

Further, details for other methods are summarized in Tbl. 1 (**kDOP**), Tbl. 2 (**OurReLUField**), Tbl. 3 (**OurNN**) and Tbl. 4 (**OurNNEarly**).

For the positional encoding mentioned in the main document, we use the well-known approach presented in [Mildenhall et al. 2021] to encode the network’s input (details in Tbl. 5). We use an encoding depth of 8, which results in the input being 18-dimensional (2D point * 8 encodings, plus the 2D input).

For point queries, the grid resolution is the same as our data size. For ray, plane and box queries, since the input is $2\times$ dimensionality, it is the data size doubled.

4 DATA

We show the 2D and 3D indicators used in Fig. 1.

5 SPEED

We provide the speed of the bounding operation for all queries (point, ray, plane and box), dimensions and methods in Tbl. 6. For each combination of dimension and query, we report the speed in milliseconds as an average over 10000 independent runs with 10 million randomly sampled queries. All methods are implemented as vectorized code to make full use of GPU acceleration on a workstation equipped with an RTX3090 GPU and Intel i9-12900K CPU.

Additionally, while the use of GPU-based libraries might incur a timing overhead, more traditional metrics like FLOPs are not suitable here either. Take, e.g., the AABB inference test for point queries, $x < x_{\max}$ & $x > x_{\min}$, which is equal to zero FLOPs, as FLOPs don’t count comparisons, logical operations or memory access, but still has a non-zero runtime. The research of more robust timing metrics to compare non-neural to neural approaches is left to future work.

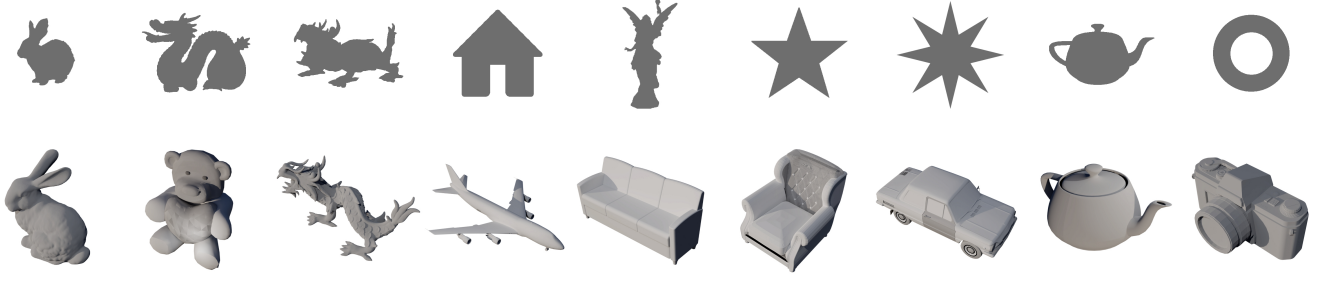


Figure 1: The 2D and 3D objects used for evaluation in the main manuscript. The 3D shapes are from ShapeNet [Chang et al. 2015] and the Stanford Computer Graphics Laboratory. We use the 2D images at resolution 32^2 and 3D shapes in voxelized form at 32^3 resolution. For the 4D sequences, the Stanford Bunny, Stanford Asian Dragon, and Utah Teapot are each rotated clockwise around their x-axis, completing a full rotation in 10 time steps.

Table 1: OurkDOP architectures, where 'k' is the number of directions.

| Result | Ind. | Query | k |
|-------------|------------|------------------------|---|
| Main Tab. 1 | 2D, 3D, 4D | Point, Ray, Plane, Box | 4 |

Table 2: OurReLUfield resolutions.

| Result | Ind. | Query | Resolution |
|-------------|------|-----------------|------------------------------------|
| Main Tab. 1 | 2D | Point | 32×32 |
| Main Tab. 1 | 2D | Ray, Plane, Box | $32 \times 32 \times 32 \times 32$ |
| Main Tab. 1 | 3D | Point | $32 \times 32 \times 32 \times 32$ |
| Main Tab. 1 | 4D | Point | $10 \times 32 \times 32 \times 32$ |

Table 3: OurNN architectures.

| Result | Ind. | Query | Network |
|--------------------------|------|-----------------|----------------------------------|
| Main Tab. 1, Main Fig. 6 | 2D | Point | $2 \times 25 \times 25 \times 1$ |
| Main Tab. 1, Main Fig. 6 | 2D | Ray, Plane, Box | $4 \times 25 \times 25 \times 1$ |
| Main Tab. 1, Main Fig. 6 | 3D | Point | $3 \times 50 \times 50 \times 1$ |
| Main Tab. 1, Main Fig. 6 | 3D | Ray, Plane, Box | $6 \times 50 \times 50 \times 1$ |
| Main Tab. 1, Main Fig. 6 | 4D | Point | $4 \times 75 \times 75 \times 1$ |
| Main Tab. 1, Main Fig. 6 | 4D | Ray, Plane, Box | $8 \times 75 \times 75 \times 1$ |

Table 4: OurNNEarly architectures.

| Result | Ind. | Query | Input | Exit1 | Exit2 |
|-------------|------|-----------------|--------------|---------------|-------------------------|
| Main Tab. 1 | 2D | Point | 2×1 | 25×1 | $25 \times 25 \times 1$ |
| Main Tab. 1 | 2D | Ray, Plane, Box | 4×1 | 25×1 | $25 \times 25 \times 1$ |
| Main Tab. 1 | 3D | Point | 3×1 | 50×1 | $50 \times 50 \times 1$ |
| Main Tab. 1 | 3D | Ray, Plane, Box | 6×1 | 50×1 | $50 \times 50 \times 1$ |
| Main Tab. 1 | 4D | Point | 4×1 | 75×1 | $75 \times 75 \times 1$ |
| Main Tab. 1 | 4D | Ray, Plane, Box | 8×1 | 75×1 | $75 \times 75 \times 1$ |

6 COMPLEXITY

From our results one can easily see that our method's advantage increases with dimensionality. We visualize this in detail in Fig. 2. This is because in concave shapes of natural high-dimensional signals, empty space grows much quicker than is intuitive. High-dimensional space is mostly empty, as the data tends to become sparse [Aggarwal et al. 2001]. This is also why neural networks (NNs) excel as classifiers and best imagined in four dimensions, space plus time, where the space-time indicator of a moving objects is highly concave but mostly empty, and well represented by a NN of low complexity: a bit of bending, and that is already much better than any box or sphere.

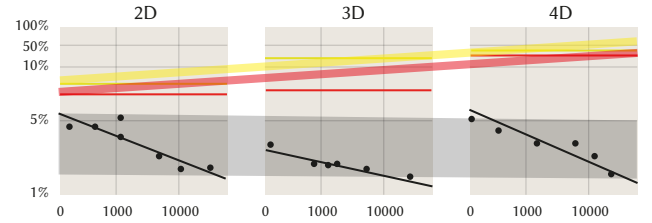


Figure 2: False positive rate in percentage (vertical axis) as a function of model complexity, i.e. number of tuned parameters (horizontal axis in each subplot) for three different dimensions (subplots). Different colors are different methods (OBox, Sphere, OurNN; baselines are constants with respect to complexity which remains fixed in each dimension). Across dimensions, we see that false-positives (FPs) increase for baselines, while for ours, the rate (still function of model complexity itself) remains roughly constant (funnels).

REFERENCES

- Charu C Aggarwal, Alexander Hinneburg, and Daniel A Keim. 2001. On the surprising behavior of distance metrics in high dimensional space. In *Database Theory*. 420–434.
- Angel X. Chang, Thomas Funkhouser, Leonidas Guibas, Pat Hanrahan, Qixing Huang, Zimo Li, Silvio Savarese, Manolis Savva, Shuran Song, Hao Su, Jianxiong Xiao, Li Yi, and Fisher Yu. 2015. *ShapeNet: An Information-Rich 3D Model Repository*. Technical Report arXiv:1512.03012 [cs.GR]. Stanford University – Princeton University – Toyota Technological Institute at Chicago.
- Ben Mildenhall, Pratul P. Srinivasan, Matthew Tancik, Jonathan T. Barron, Ravi Ramamoorthi, and Ren Ng. 2021. Nerf: Representing scenes as neural radiance fields

Table 5: Architecture details for all results shown in this paper. $a \in \{10, 16, 25, 50, 75, 125\}$, $b \in \{25, 50, 64, 75, 125, 256\}$, $c \in \{75, 125, 256, 512, 768, 1024\}$

| Result | Ind. | Query | Network | PE |
|--------------------------|------|-------|--|----|
| Main Fig. 1 | 2D | Point | $2 \times 20 \times 10 \times 5 \times 1$ | 0 |
| Main Tab. 1, Main Fig. 6 | all | all | Tbl. 1, Tbl. 2, Tbl. 4, Tbl. 3 | 0 |
| Main Tab. 2 | 3D | Ray | $6 \times 50 \times 50 \times 1$ | 0 |
| Main Fig. 10, a, b | 3D | Point | $3 \times 100 \times 100 \times 100 \times 1$ | 0 |
| Main Fig. 10, c | 3D | Point | $3 \times 50 \times 50 \times 1$ | 0 |
| Main Fig. 4 | 2D | Point | $2 \times 10 \times 1$ | 0 |
| Main Fig. 11, a | 2D | Point | $2 \times 10 \times 10 \times 1$ | 0 |
| Main Fig. 11, b | 2D | Point | $2 \times 10 \times 10 \times 5 \times 1$ | 0 |
| Main Fig. 11, c | 2D | Point | $2 \times 25 \times 25 \times 5 \times 1$ | 0 |
| Main Fig. 11, d | 2D | Point | $2 \times 128 \times 128 \times 128 \times 1$ | 18 |
| Fig. 2, 2D | 2D | Point | $2 \times a \times a \times 1$ | 0 |
| Fig. 2, 3D | 3D | Point | $3 \times b \times b \times 1$ | 0 |
| Fig. 2, 4D | 4D | Point | $4 \times c \times c \times 1$ | 0 |
| Main Fig. 5 | 2D | Point | $2 \times 10 \times 10 \times 10 \times 1$ 3 exits | 0 |
| Main Fig. 12 | 12D | Point | $12 \times 25 \times 25 \times 1$ | 0 |
| Main Fig. 9, hit | 3D | Point | $3 \times 40 \times 40 \times 1$ | 0 |
| Main Fig. 9, no-hit | 3D | Point | $3 \times 100 \times 100 \times 100 \times 1$ | 0 |

Table 6: Query speed of methods in ms, averaged across 10,000 independent runs with 10 million samples per run.

| | 2D | | | | 3D | | | | 4D | | | |
|------------|-------|-------|-------|-------|-------|-------|-------|-------|--------|--------|--------|--------|
| | Point | Ray | Plane | Box | Point | Ray | Plane | Box | Point | Ray | Plane | Box |
| AABox | 1.03 | 2.08 | 2.08 | 2.08 | 1.27 | 2.58 | 2.58 | 2.58 | 2.04 | 4.21 | 4.21 | 4.20 |
| OBox | 1.03 | 2.08 | 2.09 | 2.09 | 1.27 | 2.58 | 2.59 | 2.60 | 2.06 | 4.22 | 4.24 | 3.42 |
| Sphere | 1.06 | 1.85 | 1.85 | 1.85 | 1.31 | 2.36 | 2.36 | 2.38 | 1.83 | 3.43 | 3.43 | 3.42 |
| AAElli | 1.07 | 1.86 | 1.86 | 1.86 | 1.33 | 2.39 | 2.39 | 2.44 | 1.84 | 3.46 | 3.46 | 3.46 |
| OElli | 1.07 | 1.87 | 1.86 | 1.87 | 1.33 | 2.39 | 2.45 | 2.43 | 1.84 | 3.46 | 3.47 | 3.47 |
| kDOP | 12.42 | 14.36 | 14.37 | 14.35 | 10.61 | 41.27 | 41.40 | 41.39 | 14.06 | 54.84 | 54.87 | 54.66 |
| BVH | 18.06 | 23.28 | 22.96 | 23.42 | 17.40 | 25.67 | 26.35 | 26.13 | 24.52 | 29.17 | 27.09 | 25.10 |
| OurkDOP | 4.41 | 7.73 | 7.72 | 7.72 | 5.64 | 11.84 | 11.76 | 11.70 | 7.79 | 16.58 | 16.56 | 16.53 |
| OurNN | 28.14 | 28.43 | 28.44 | 28.43 | 70.32 | 70.82 | 70.74 | 70.69 | 111.90 | 113.08 | 112.79 | 112.58 |
| OurNNEarly | 24.55 | 29.26 | 32.39 | 30.71 | 35.97 | 46.30 | 74.70 | 50.90 | 64.86 | 96.15 | 135.08 | 101.95 |